Suppression of Random Coincidences During In-Beam PET Measurements at Ion Beam Radiotherapy Facilities

Paulo Crespo, Thomas Barthel, Helmut Frais-Kölbl, Erich Griesmayer, *Member, IEEE*, Klaus Heidel, Katia Parodi, Jörg Pawelke, and Wolfgang Enghardt

***Abstract*—In-beam positron emission tomography (PET) is currently the only method for an *in-situ* monitoring of charged hadron therapy. However, in-beam PET data, measured at beams with a sub-μs-microstructure due to the accelerator radio frequency (RF), are highly corrupted by random coincidences arising from prompt γ rays following nuclear reactions as the projectiles penetrate the tissue. Since random-correction techniques from conventional PET cannot be applied, the clinical in-beam PET at the therapy facility at the Gesellschaft für Schwerionenforschung (GSI), Darmstadt, Germany, merely reconstructs events registered in the pauses ($\sim$ 2–4 s) between the beam macropulses ($\leq$ 2 s). We have successfully tested two methods for suppressing the micropulse-induced random coincidences during beam extraction. Image statistics can be increased by about 90%. Both methods rely on the synchronization of the $\gamma\gamma$ coincidences measured by the positron camera with the time microstructure of the beam, either by using the RF signal from the accelerator or the signal of a thin diamond detector placed in the beam path in front of the target. Energy and triple-coincidence time-correlated spectra first measured during beam extraction, combined with the corresponding tomographic images of the β^+ activity induced by the beam in a plastic phantom, clearly confirm the feasibility of the proposed random suppression methods. These methods provide the solution for applying in-beam PET at synchrotron and cyclotron radiotherapy facilities with optimal use of the annihilation photon flux.**

***Index Terms*—Avalanche photodiode (APD), ion therapy, LSO, positron emission tomography (PET), proton therapy.**

I. Introduction

THE TERM *in-beam PET* denotes the use of positron emission tomography (PET) to image the β^+ activity distributions induced in the target volume during patient irradiation [1]. This is currently the only method for an *in-situ* monitoring of the particle delivery in hadron tumor therapy (Fig. 1). It is clinically applied to the carbon ion tumor irradiation at the Gesellschaft für Schwerionenforschung (GSI) in Darmstadt, Germany. There, over 240 patients with radioresistant tumors in the head and neck region or in the spinal cord have been irradiated since December 1997, yielding very promising clinical results [2], [3]. Six years of clinical application have proven the technical feasibility of operating an in-beam PET scanner for monitoring therapeutic irradiation with ion beams. Although the implementation of safety margins around the tumor and the selection of proper beam portals minimize the clinical effect of deviations from treatment planning, in-beam PET is able to detect possible range or portal deviations, as well as anatomical modifications during fractionated irradiation [1].

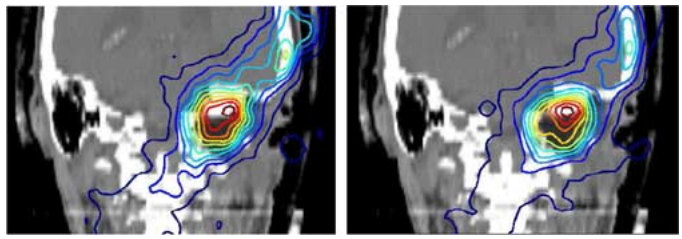

Fig. 1. In-beam PET. β^+ activity distribution expected from the treatment plan (left) versus measured (right) for one patient suffering from a skull base tumor and treated with carbon ion therapy. The distributions are superimposed onto the patient's X ray computed tomogram. Note the sparing of the brainstem in both the expected as well as the measured distributions.

The counting statistics of in-beam PET images is generally low, and limited by the applied dose. Typical activity densities induced at the fractionated tumor therapy irradiation reach about 200 Bq cm^{-3} Gy^{-1}, with the dose per portal ranging between 0.3 and 1 Gy. This contrasts with activity density values of 10^4 to 10^5 Bq cm^{-3} in human PET tracer imaging, and even 10^6 Bq cm $^{-3}$ in animal PET studies. For a given detector geometry, the only way to improve image quality is the efficient use of the annihilation photons available. Current limitations arise from the fact that in-beam PET data, measured at beams with a sub-μs-microstructure due to the accelerator radio frequency (RF), are highly corrupted by random coincidences. These arise from prompt γ rays following nuclear reactions of the projectiles with the atomic nuclei of the tissue. They cannot be suppressed with random-correction techniques from conventional PET [4], [5]. Therefore, at the GSI treatment facility, in-beam PET images are reconstructed, taking into account events registered in the pauses ($\sim$ 2–4 s) between the beam macropulses ($\leq$ 2 s, Fig. 2).

Manuscript received November 9, 2004; revised March 9, 2005. This work was supported in part by the Bundesministerium für Bildung und Forschung of Germany, in part by the Ministerium für Wissenschaft und Kunst of the Free State of Saxony, Germany, and in part by the Gesellschaft für Schwerionenforschung, Darmstadt, Germany.

P. Crespo, K. Heidel, J. Pawelke, and W. Enghardt are with the Forschungszentrum Rossendorf, Institute of Nuclear and Hadron Physics, 01314 Dresden, Germany (e-mail: crespo@fz-rossendorf.de; k.heidel@fz-rossendorf.de; j.pawelke@fz-rossendorf.de; w.enghardt@fz-rossendorf.de).

T. Barthel was with the Forschungszentrum Rossendorf, Institute of Nuclear and Hadron Physics, 01314 Dresden. He was also with the Hochschule Mittweida, University of Applied Sciences, 09648 Mittweida. He is now with the Klinikum Chemnitz gGmbH, Klinik für Radioonkologie, 09113 Chemnitz, Germany (e-mail: t.barthel@skc.de).

H. Frais-Kölbl and E. Griesmayer are with the MedAustron and FOTEC, 2700 Wiener Neustadt, Austria (e-mail: frais@fhwn.ac.at; eg@fotec.at).

K. Parodi was with the Forschungszentrum Rossendorf, Institute of Nuclear and Hadron Physics, 01314 Dresden, Germany. She is now with the Massachusetts General Hospital, 02114 Boston, MA, USA (e-mail: kparodi@partners.org).

Digital Object Identifier 10.1109/TNS.2005.852637

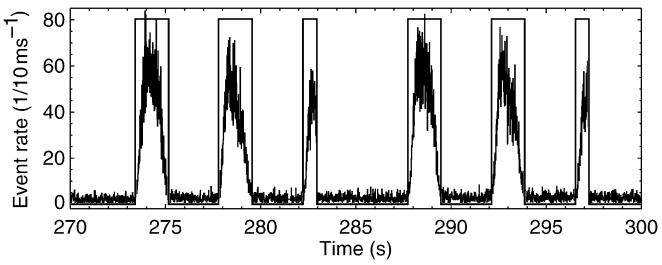

Fig. 2. Correlation between the beam delivery and the coincidence event rate during an in-beam PET scan. The rectangular graph denotes the extraction signal: low during beam acceleration (no particle delivered, data reconstructed), high during the beam macropulses (data discarded for reconstruction).

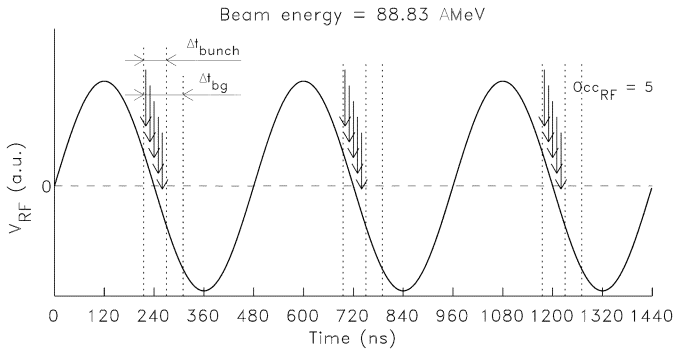

Fig. 3. Correlation between the moment of particle arrival (illustrated schematically with arrows) and RF phase (arbitrarily set to π), depicted for a given beam energy and intensity (10^7 ions/s). The RF occupancy $\mathrm{occ_{RF}}$ is 5 ($\mathrm{occ_{RF}} = I \cdot T_{\mathrm{RF}}$, with I the beam intensity).

An increase in image statistics of up to 65% is expected if coincidences acquired during the macropulse, but out of the micropulses, can be taken into account [6]. Two methods for suppressing the micropulse-induced random coincidences have been successfully tested with carbon ions at the medical beam line at GSI, and are described here.

II. Methods for Random Correction

It has been shown that the noise introduced by random coincidences is an important limiting factor of count-rate performance for PET cameras operating in three-dimensional (3-D) mode [7]. The number of random coincidences on a particular line-of-response (LOR) can be corrected in conventional PET, following either the delayed-coincidence method or the singles-count-rates method. The delayed-coincidence method is more common in the current generation of cameras. It assumes the measured prompt count rate C_m at a given LOR to be the sum of the true coincidence count rate C_t with the random count rate C_r, provided C_r is stationary in time. C_r is measured at a time significantly greater than the coincidence-resolving time of the detectors, and subtracted from C_m for each LOR. In the singles-count-rates method, singles rates from each individual detector element are collected and used to account for the random count rate of each LOR with the relation

$$C_r = 2\Delta t C_i C_j \tag{1}$$

where C_i and C_j are the singles-count rates in detectors i and j, forming LOR ij, and 2 Δt is the coincidence-time resolution.

The application of both methods to in-beam PET fails because C_r is not constant in time during particle extraction due to the existence of a microstructured beam delivery [5].

A. The Time Microstructure of the Beam

During beam extraction, a correlation between the moment of arrival of the ions and a given phase of the RF signal from the accelerator has been found [5]. This correlation is depicted in Fig. 3 for a given beam energy and intensity (10^7 ions/s). During each RF period T_{RF}, the ions arrive within a time window $\Delta t_{\mathrm{bunch}}$. The width of this window is dependent on the beam energy and, therefore, on T_{RF}, and independent of the beam intensity up to the maximum therapy intensity (2×10^8 ions/spill).

At the tumor therapy unit at GSI, ^{12}C beam energies range from 88.83 to 430.10 *A*MeV, corresponding to T_{RF} from 480 down to 250 ns, respectively. The correlation between T_{RF} and beam relativistic kinetic energy K is given by

$$T_{\mathrm{RF}} = \frac{P_{SIS} \cdot f(K)}{n_{SIS} \cdot c} \cdot \frac{K + m_o c^2}{\sqrt{K^2 + 2K m_o c^2}} \tag{2}$$

with values and units described in Table I. The particle trajectory factor $f(K)$ arises from the different oscillations about the synchrotron perimeter that the particles undergo for a given energy, with $f(K)$ decreasing with increasing energy.

TABLE I
Parameters Correlating Beam Energy and RF Period

Perimeter of synchrotron	P_{SIS}	216 m
Particle trajectory factor	$f(K)$	1.091 to 1.008
Number of concomitant bunches	n_{SIS}	4
Speed of light in vacuum	c	2.998 $\times 10^8$ m/s
Energy per nucleon	E	88.8 to 430.1 *A*MeV
Total kinetic energy	$K = 12 \cdot E$	1.1 to 5.2 GeV
Rest mass of ^{12}C	m_o	11 178 MeV/c^2

The time window $\Delta t_{\mathrm{bunch}}$ comprises the time slot in which the ions arrive at each RF cycle. During this time, and shortly after it (Δt_{bg} in Fig. 3), a high flux of γ rays, arising from nuclear reactions when the ions penetrate the target, is emitted [5]. This sub-μs periodic flux constitutes the source of the high, in-beam random rate, and any in-beam random suppression method must be able to discard it.

B. Methods Proposed for In-Beam PET

Two methods have been proposed which allow for identifying coincident events occuring within the time window Δt_{bg} [6], and are depicted in Fig. 4.

1) Using the RF-Signal From the Accelerator: If each $\gamma\gamma$ coincidence detected with the positron camera is correlated with the phase of the RF signal, those events occuring within Δt_{bg} can either be labeled for posterior elimination, or immediately discarded by the acquisition electronics (DAQ). In this first proof-of-principle approach, we have chosen to register all events in list mode [8] and process them offline, in order to store the maximum of information and to preserve the full flexibility for data evaluation. This was necessary in order to

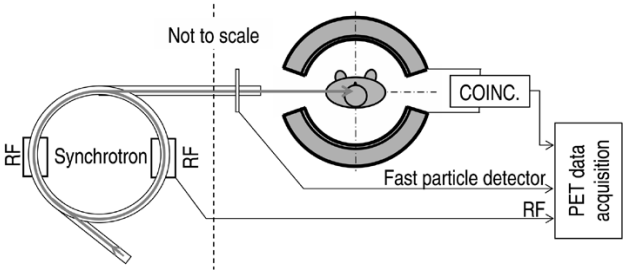

Fig. 4. Implementation of the methods proposed for in-beam PET random correction. Every detected $\gamma\gamma$ coincidence is correlated with the incoming ion by using either an FD or the RF signal from the accelerator.

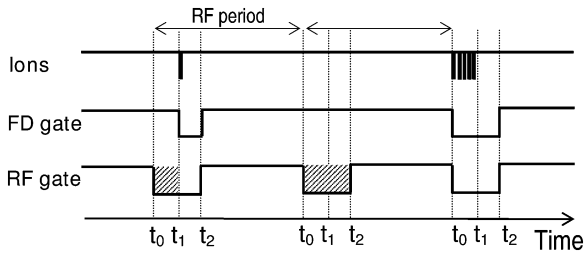

Fig. 5. Different timing windows, automatically adjusting to the RF occupancy, are implementable with an FD, in contrast to the fixed-length, RF-generated windows.

implement a proper timing selection around Δt_{bg}, since coincidence measurements between $\gamma\gamma$ events and the RF phase had not been performed before.

2) Using a Fast Particle Detector: A second method of labeling coincidences arriving during the microbunches makes use of a thin, fast particle detector (FD) placed in the beam path in front of the target. In principle, and for low-RF occupancies, this approach should allow the implementation of narrower time windows around Δt_{bg} when compared with the RF method, as depicted in Fig. 5. As it can be seen, the FD method does not trigger a gate unless a particle arrives, leading to higher readout available time in the case of low $\mathrm{occ_{RF}}$.

III. Implementation: Setup and Electronics

The two methods described were simultaneously implemented with the system depicted in Fig. 6. For the detection of a given RF phase, a very fast peak detector NIM module (phase trigger) was developed at the Forschungszentrum Rossendorf (FZR), Dresden, Germany. For ion arrival detection, we have used a 300-μm thick, chemical vapor deposition (CVD) diamond detector [9] developed and optimized at the Forschungs- und Technologietransfer GmbH (FOTEC), Wiener-Neustadt, Austria. Furthermore, two position-sensitive scintillation detectors, each consisting of 32 crystals ($2.1 \times 2.1 \times 15$ mm^3) of cerium-doped lutetium oxyorthosilicate (LSO) coupled to the 4×8 pixels of an avalanche photodiode array (APDA) [10], were operated in coincidence, and limited-angle in-beam tomographic imaging was performed following the method described in [11]. In short, a phantom of polymethylmethacralate (PMMA) stopping the beam was placed between the detectors and was scanned parallel to the beam axis. This allowed retrieving 2-D images and linear profiles of the positron emitter depth distribution under several regimes (e.g., during the extraction pauses or during the beam extraction, inside and outside the microbunches). For every detected $\gamma\gamma$ coincidence (trigger: time window of TAC1), a readout of the energy signal in all imaging pixels (64) is performed, which allows for applying energy selection during offline data evaluation. Further, the time differences between the detected $\gamma\gamma$ coincidence and the RF phase (TAC3: $\gamma\gamma$-RF), as well as the particle crossing the diamond detector (TAC2: $\gamma\gamma$-ion), were read. The accelerator status was also recorded by sampling the extraction signal.

IV. Results and Discussion

A. Detectors for Synchronization With the Beam Microstructure

1) Phase Trigger: This module proved to be a good first solution for the detection of a given RF phase, since the long cabling between the SIS and the experiment place (medical cave) introduced baseline oscillations of $\pm 10\%$ of the RF amplitude. A time measurement between consecutive RF periods at fixed beam energy revealed that the phase trigger was nearly insensitive to these oscillations (measured deviations were less than 1%). Despite performing well at a fixed beam energy, this capacitor-based peak detector introduces frequency-dependent delays that have to be improved before the phase trigger can be used with the consecutively changing energies during therapeutic irradiations by means of the GSI rasterscan beam delivery [12].

2) CVD Diamond Detector: Fig. 7 shows the in-beam performance of the CVD detector when 200.2 *A*MeV carbon ions trespass it at a beam intensity of 10^8 ions/s, corresponding to an $\mathrm{occ_{RF}}$ of about 32 ions/bunch. The analog signal in Fig. 7 shows that the detector is capable of identifying single ions, but due to the 3 MHz low cutoff frequency [9] introduced by the 1 nF capacity placed between the fast amplifiers (Fig. 6), the shaping electronics deliver a signal with undershoot and pulse pileup. Furthermore, saturation of the last amplifying stage also occurred due to the high current induced by the high ion flux in the middle of the microbunch. For these reasons, the measurements obtained with the CVD detector present noisier time spectra and spatial profiles, as exemplified in Section IV-B. Besides this fact, the results with the diamond detector are identical in all aspects to those obtained with the phase trigger [13] and, therefore, only the latter are presented.

B. Time and Energy Correlation Between $\gamma\gamma$, $\gamma\gamma$-RF, and $\gamma\gamma$-Ion

A clear correlation between the $\gamma\gamma$ coincidences and the beam microstructure was observed with both methods, and is shown in Fig. 8 for the RF measurements. This correlation can first be seen in column 1, where all events arriving within a time window of about 20 ns are plotted. The energy threshold was set by hardware individually for each pixel at about 300 keV. The $\gamma\gamma$ time spectrum is deteriorated by randoms, in comparison with the same spectrum in the extraction pauses (column 4), and the $\gamma\gamma$-RF time spectrum shows a peak above a constant plateau, indicating the elevated event rate during the microbunches [5]. After setting an energy window for the photon detectors (column 2), the peak-to-plateau ratio in the

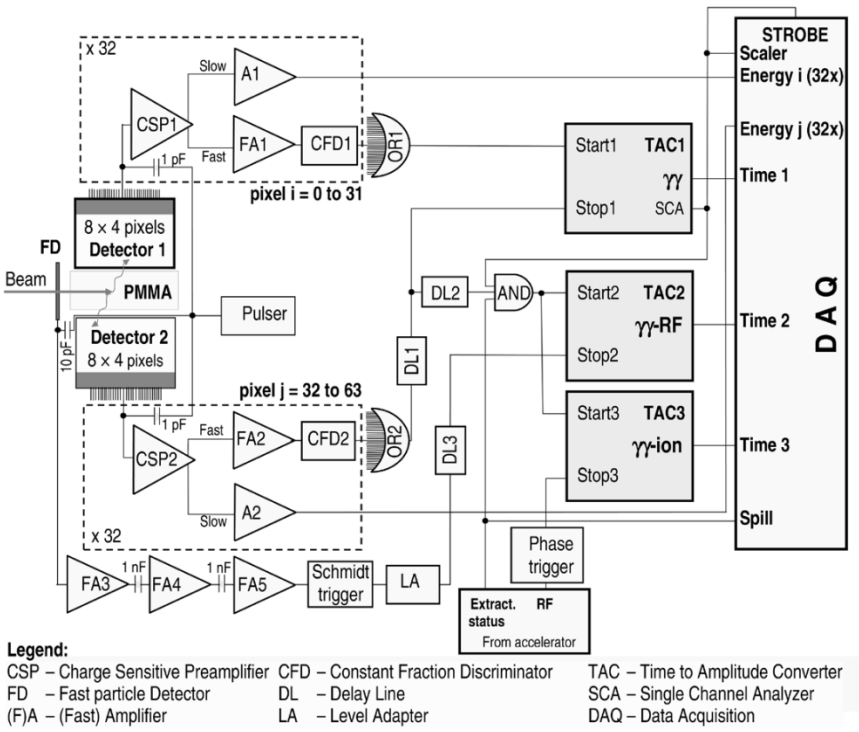

Fig. 6. Scheme of the experimental setup, the event trigger, front-end, and signal-processing electronics implemented.

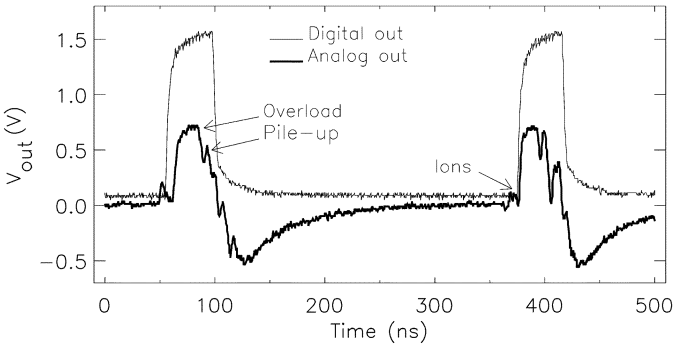

Fig. 7. Analog (after three amplification stages) and digital outputs of the diamond detector during two microbunches with an occupancy of ~ 32.

$\gamma\gamma$-RF time spectrum decreases more than one order of magnitude. If only photopeak-coincident photons [within the full width at half maximum (FWHM)] are considered, the $\gamma\gamma$-RF peak almost vanishes (column 3), and the $\gamma\gamma$ time spectrum approaches the shape seen in the extraction pauses. This indicates that the large peak in the $\gamma\gamma$-RF time spectra originates indeed from prompt nuclear decay, and not from positron annihilation.

The $\gamma\gamma$-RF time spectrum of Fig. 8 (column 1, B_1), showing a measured Δt_{bg} of 30 ns FWHM, also allows concluding that $\Delta t_{\text{bunch}} \cong \Delta t_{bg}$ at the used beam energy, since a measurement showing $\Delta t_{\text{bunch}} = 32$ ns was performed in [5].

The results obtained with the diamond detector are similar but much noisier, as shown in Fig. 9.

C. DAQ Dead Time

The system dead time τ over the whole measurement was 57.4%. This value includes the dead times of two different measuring regimes that can be clearly separated (Fig. 2): the extraction pauses with low count rate, and consequently, low DAQ dead time ($\tau_{\text{pause}} \sim 1.2\%$), and events aquired during beam extraction with higher DAQ dead time ($\tau_{\text{ext}} \sim 58.8\%$). The same separation cannot be achieved during beam extractions (within microbunch, B, or not, A), because the signal and readout of each event overlays several RF periods. For this reason, even the low-rate events taking place outside Δt_{bg} (A) present a high dead time close to 58.8%. A more detailed analysis can be found in [13].

D. Tomographic Imaging and Quantification of Image Gain

The activity distributions obtained with a photon energy window between 300 and 850 keV are plotted in Figs. 10 and 11 for three beam-delivery regimes: extraction pauses (P), during extractions but out of Δt_{bg} (A_2), and during extractions but inside Δt_{bg} (B_2). In both figures, it can be seen that the events acquired within the microbunch (B_2) exhibit a typical random behavior, presenting a nearly constant spatial distribution (Fig. 10, top) corresponding to a plateau (Fig. 11, curve B_2) declining beyond the primary particle range, i.e., outside the region where the nuclear reactions predominantly take place. The small, but noticeable, increase at about 68 mm arises from β^+ decays taking place within Δt_{bg} which, consequently, cannot be separated (Fig. 8). In contrast, events acquired outside Δt_{bg} reproduce the characteristic β^+ distribution (Fig. 10, middle) and depth profile (Fig. 11, curve A_2) of the irradiation-induced activity rather well (Fig. 10, bottom, and Fig. 11, curve P).

For image quantification, the geometrical solid angle of the two coincident detectors was simulated. This was done by starting 10 million events at the image center and registering the fraction of events impinging onto two opposing crystals along one LOR, yielding $\Omega_{\text{LOR}} = 2.3 \times 10^{-4}$. Due to the

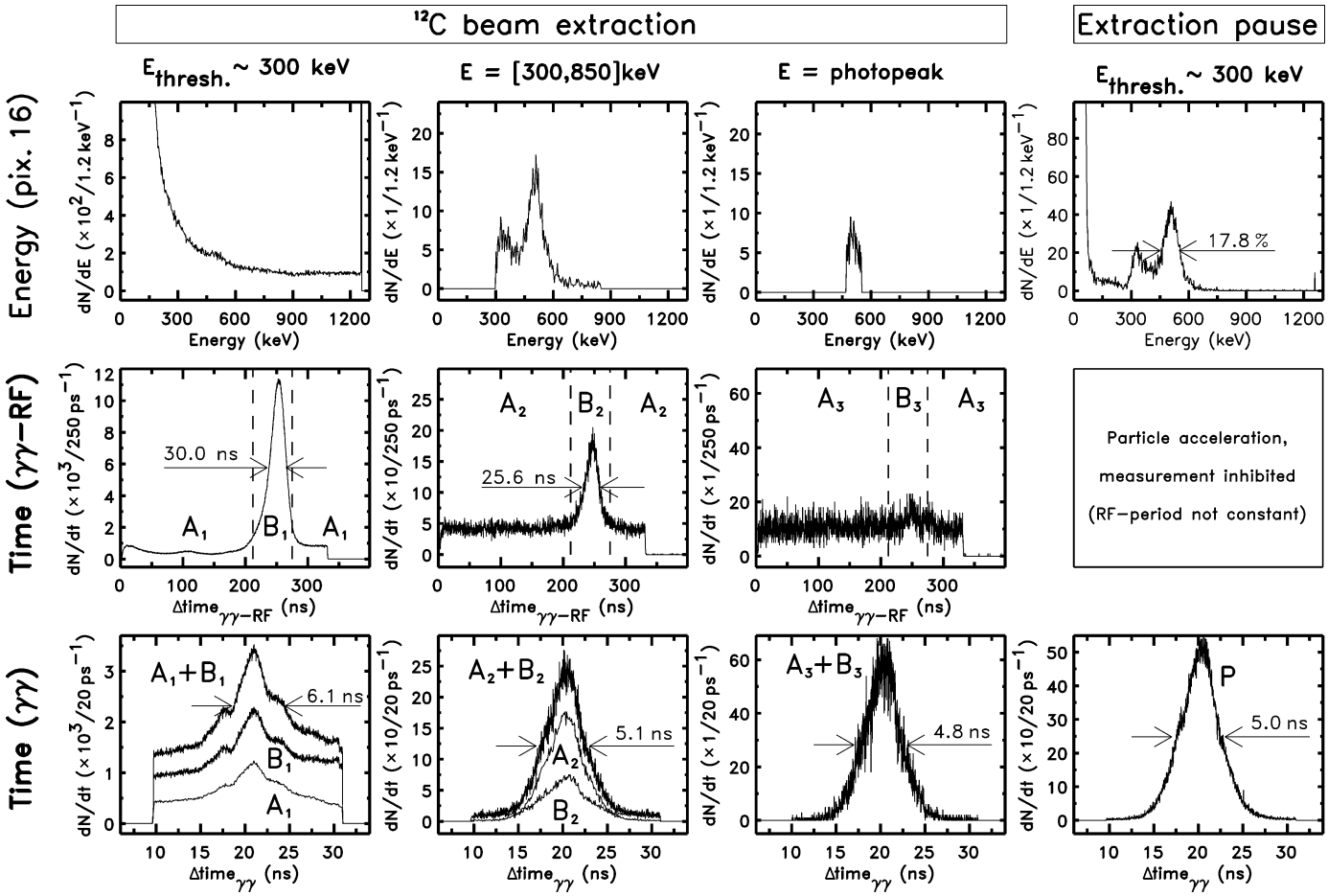

Fig. 8. Results of $\gamma\gamma$-RF coincidence measurements during ^{12}C beam extraction. The $\gamma\gamma$ coincidence time spectra (lower row) have been constructed by setting different sorting conditions in the γ ray energy spectra (upper row) and the $\gamma\gamma$-RF time distributions (middle row). As reference, γ ray energy and coincidence time spectra acquired in the beam extraction pauses are additionally shown (column 4). The energy selection in columns 1 and 4 was implemented by hardware, and consequently, low-energy events below threshold can be seen, arising from a low-energy readout when any other pixel is triggered. In columns 2 and 3, the accepted energy window was applied by software during data analysis.

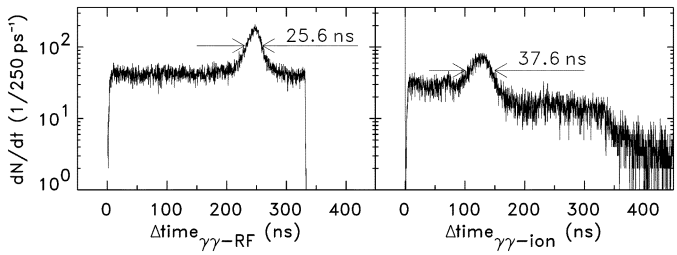

Fig. 9. Triple-coincident time spectra. $\gamma\gamma$ RF (left) and $\gamma\gamma$ ion (right, measured with the diamond detector). Both spectra correspond to $\gamma\gamma$ events within an energy window of 300–850 keV.

much longer distance between detectors (112 mm) in respect to detector front size (18.4×9.2 mm^2), the central solid angle $\Omega_{\odot}$ follows by multiplication of Ω_{LOR} with the total number of LOR (32). The total coincidence-detection efficiency ϵ_{tot} of the two opposing detectors is given by

$$\epsilon_{\mathrm{tot}} = \Omega_{\odot} \cdot \epsilon_{\mathrm{LOR}} \cdot \overline{\Omega_{r,\odot}} \cdot P_{\gamma\mathrm{esc}} \tag{3}$$

with ϵ_{LOR} the efficiency of coincidence photon detection in the LSO for one LOR. With the photon energy window implemented, ϵ_{LOR} amounts to 18.1%. The term $\overline{\Omega_{r,\odot}}$ represents the mean relative solid angle of each image voxel with respect to the central voxel (30%), as determined by flood source measurements. The term $P_{\gamma\mathrm{esc}}$ quantifies the probability for double escape of the 511 keV γ rays from the phantom: 15.2%.

The simulation of the expected number of counts was achieved with the PosGen Monte Carlo code [14], yielding a total of 1.98×10^7 β^+ decaying nuclei produced per spill ($2\times10^8$12$^{\mathrm{C}}$ ions with 200.2 AMeV). The expected total number of counts $C^{(j)}$ from the decay of isotope j with half-life $T_{1/2}^{(j)}$ follows by integrating the initial activity A_0^j induced per spill over 300 extraction cycles (5-s period) and amounts to

$$C^{(j)} = A_0^{(j)} \frac{T_{1/2}^{(j)}}{\ln 2} \sum_{i=0}^{299} \left[1 - \exp\left(\frac{1500s - i \cdot 5\,\mathrm{s}}{\frac{T_{1/2}^{(j)}}{\ln 2}} \right) \right]. \tag{4}$$

The calculation of the simulation curve in Fig. 11 takes into account only acquisitions in the extraction pauses. The isotopes ^{11}C, ^{10}C, ^{15}O, and ^{13}N, with half-lives larger than a few seconds, were considered, and the total events detected were multiplied by 3/5 (timing weight of the extraction pauses).

The relative improvement in image counts ΔC_r was calculated to be $\leq 90\%$ by taking into account the coincidences measured during beam extraction, outside the microbunches (image

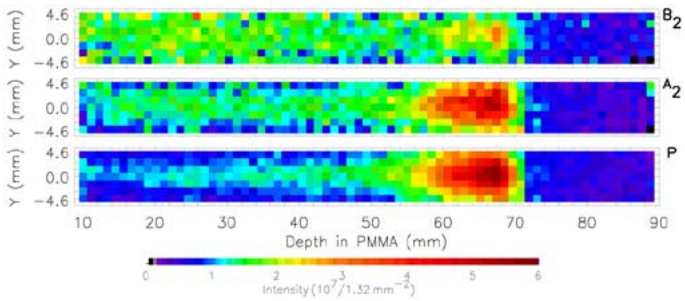

Fig. 10. Longitudinal tomograms of the activities generated by stopping the beam in a PMMA phantom, and obtained with the $\gamma\gamma$ RF method (top and middle only). The γ ray energy window is 300–850 keV. The symbols P, A_2, and B_2, also described in the text, refer to Fig. 8.

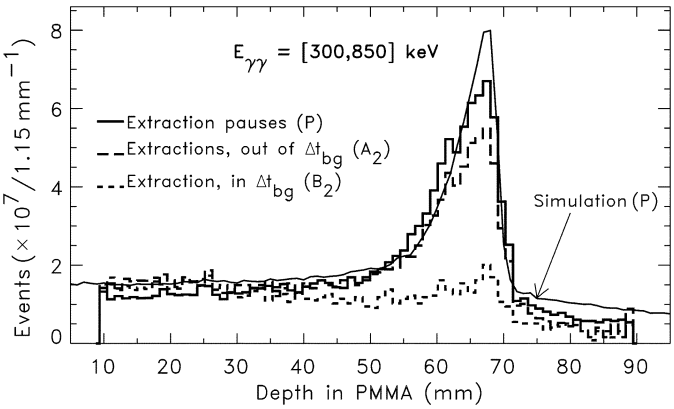

Fig. 11. Depth profiles between the detectors obtained with the $\gamma\gamma$ RF method. The simulation curve (extraction pauses) is left-shifted by 4 mm to compensate for the ion energy loss in the diamond detector and its copper housing.

TABLE II
RELATIVE INCREASE IN IMAGE STATISTICS DEDUCED FROM THE β^+ ACTIVITY DEPTH DISTRIBUTIONS

Energy window	ΔC_r (maximum)	ΔC_r (8.8 - 90 mm)	ΔC_r (0 - 90 mm)
300 - 850 keV	78 %	88 %	90 %
Photopeak (2×FWHM)	73 %	75 %	78 %

A_2, Fig. 10), to the number of events measured during the extraction pauses (image P, Fig. 10). This ratio is dependent on the width of the energy window applied, as well as on the beam energy. Table II summarizes results.

The values of ΔC_r corresponding to a depth in PMMA of 0–90 mm were obtained by extrapolation, assuming a constant plateau of activity between 8.8 mm (beginning of image) down to 0 mm (beginning of phantom, not imaged). The higher relative increase in image statistics obtained with respect to the 65% estimated in [6] is suspected to originate from the contribution of short-lived, β^+ decaying isotopes that are detected with high efficiency during the beam extractions for the first time. According to the simulation [14], and correcting for the measuring time of 25 min by using (4), the most abundant are ^{12}N ($T_{1/2} = 11$ ms) and ^{8}B ($T_{1/2} = 770$ ms), contributing 9.9% and 2.1% to the total number of annihilation events, respectively. Note also the higher image blurring at the entrance plateau of activity in Fig. 10 (middle, A_2) due to the higher β^+ endpoint energy of these isotopes (16.6 and 3.3 MeV, respectively).

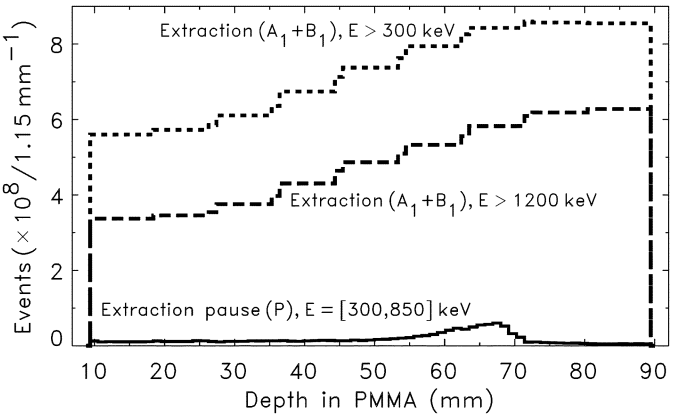

Fig. 12. Depth profiles of coincident events with higher energy values registered during beam extractions. The profiles show the average of the events seen by the full detector, rather than a pixel-based backprojection, due to the impossibility of energy discrimination above 1200 keV (ADC overload, Fig. 8). The profile measured during the extraction pauses is also shown for comparison.

E. Higher Energy Events

Due to its influence on the system dead time and on the count rates achieved, the depth profiles of coincidences with energy values above 300 keV and above 1200 keV were analyzed (Fig. 12). It can be seen that the typical random or β^+ activity profiles of Fig. 11 are substituted by profiles with counts increasing with the penetration depth, suggesting the detection of events emitted preferentially in the forward direction [5]. Although it is known that a flux of particles (mainly protons and neutrons, but also other light nuclei [15]) escapes the target volume, mainly in the forward direction, it is not clear whether the observed profiles arise from γ rays, particles, or both. An analysis of the event hit patterns onto the detectors, though, strongly suggests the passage of charged particles through the detectors in a longitudinal direction along the beam [13]. These particles could have their origin both inside the phantom and on the diamond detector and its housing, trespassed upbeam. These results indicate the strong necessity of setting an upper energy threshold close to 511 keV.

F. Event Rates

The obtained increase in image statistics is valid for the present beam-delivery system with a duty factor D_f of 40%, with

$$D_f = \frac{\Delta t_M}{T_M} \tag{5}$$

Δt_M being the macropulse duration (beam extraction, 2 s), and T_M being the time of a synchrotron acceleration cycle, comprising beam injection, acceleration, and extraction (5 s). In order to estimate the gain in collected events for therapeutic beams delivered with other accelerators with different D_f and microstructure timings, the knowledge of the event count rates calculated in the phantom is necessary. Fig. 13 shows this event rate, with the number of events collected in each regime divided by the total length of the time window in which it was collected. An extrapolation of these results to a PET system with larger solid angle is only feasible in the case of the curves showing the

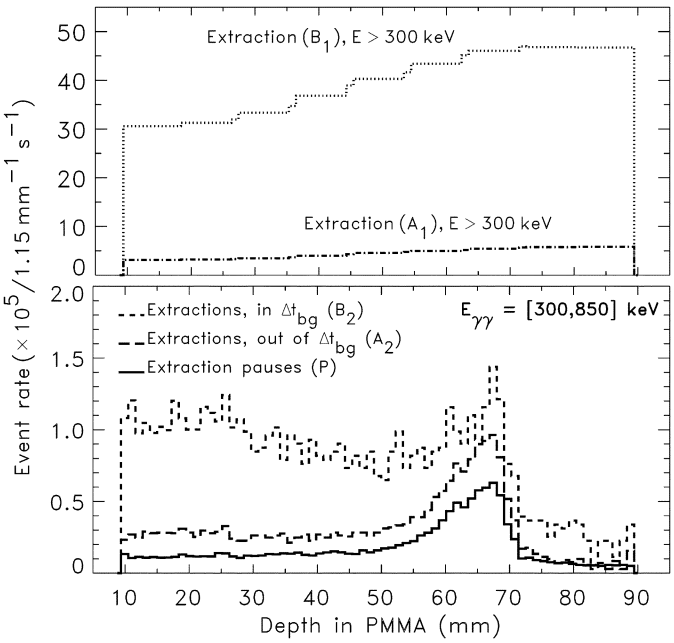

Fig. 13. Event rates versus depth in different regimes. Corrected for the solid angle of the detectors assuming isotropic event emission. The high event rate during beam extraction is remarkable.

isotropic, β^+ decaying events (P and A_2). The remaining curves regard anisotropic fluxes and will, of course, yield count rates and image deterioration dependent on the position of the detectors [5], [11].

G. Detector Performance

The results obtained are related to the properties of the imaging detectors, and any in-beam PET implementation must carefully consider these properties. Therefore, we present the main performance parameters of the detectors used.

1) Stability: This experiment required operating the detectors one year after their last in-beam experiment, and one-and-one-half years after their initial setup. We have found two pixels working inappropriately. Correct energy spectra could only be acquired at the expense of extreme amplifier gain, and timing with these two pixels was not possible. We attribute this to insufficient coupling of the scintillators to the surface of the APDA, probably due to the exposure of the detectors to the vibrations during their long transport between FZR and GSI. We conclude, therefore, that silicon glue and teflon tape [10] provide a good, long-lasting solution for manufacturing these detectors.

2) Energy and Time Resolution: Because time resolution was an important issue during these measurements, we operated the APDA with an internal gain of 70 instead of 50 in [11]. As expected, the timing performance of the two LSO/APDA detectors improved to 5.0 ns FWHM versus 6.2 ns FWHM in [11] at the cost of worse energy resolution: $16.5 \pm 0.3\%$ FWHM versus $15.5 \pm 0.3\%$ FWHM in [11].

3) Interpixel Crosstalk: An interpixel crosstalk of about 10% was observed, meaning that a 511 keV photon fully depositing its energy in a given pixel leaves a signal of ~ 50 keV in its neighboring pixels due to optical crosstalk only. The reasons for this are the noncomplete light isolation of the teflon tape surrounding the LSO crystals and, more importantly, light sharing at the LSO-diode coupling, mostly due to the common, thick expoxy layer covering all diodes [13]. Interpixel crosstalk plays a role in estimating count rates, since high-energy events (e.g., a 5 MeV signal from a crossing particle) may leave in its neighbor a false signal ($\sim$ 500 keV). In this experiment, all pixels were read and analyzed, thus crosstalk events are automatically rejected. Future applications must apply either the same principle, or a hardware energy selection that is able to reject a full cluster of pixels once a high-energy event is detected in one of them.

V. Application to Radiotherapeutic Beams

The applicability and usefulness of the methods presented depend on the timing characteristics of the therapeutic beam where the methods are to be applied. The importance of random suppression during in-beam PET measurements increases as the accelerator duty factor D_f also increases. For example, linear accelerators for electron, photon, and even ion [16] radiotherapy have extremely small duty factors ($\sim 0.1\%$), and consequently, the random suppression method described in [1] is sufficient for in-beam PET at these machines. In contrast, isochronous and superconducting cyclotrons used for ion radiotherapy [17]–[19] deliver continuous wave (CW) beams ($D_f \cong 100\%$), which renders in-beam PET implementable only if the present random suppression methods are applied. Synchrotron-delivered radiotherapeutic beams have duty factors between 10% and 90% [12], [20]–[22], meaning that such facilities can greatly profit from the application of the random suppression techniques presented here.

A. Implementation at GSI and at the Heidelberg Clinics

A mean RF occupancy of 13.9 ^{12}C ions per bunch was calculated for the GSI facility by considering all combinations of beam energies and intensities used to treat all patients to this date. Extrapolating these values to the synchrotron parameters at the future ion therapy facility in Heidelberg with an even higher duty factor yields $\overline{\mathrm{occ_{RF}}} = 8.0$. This value indicates that there may be an advantage (from the point of view of timing) in using the $\gamma\gamma$-ion with respect to the $\gamma\gamma$-RF method for this facility. Finally, the $\gamma\gamma$-ion method is easier to implement, since it does not require a correction for the transit time of the ions in the beam pipeline, which is dependent on beam energy, but has the drawback of additional material in the beam path. This becomes an advantage if the same detector could be used as a beam monitor [23].

B. Cyclotron-Delivered Therapeutic Ion Beams

In-beam PET implementation at cyclotron-based facilities seems to be nontrivial, due to the small time differences between Δt_{bg} and T_{RF}, with Δt_{bg} ranging from 0.3 ns [18] to about 6 ns [19], and T_{RF} from about 10 ns [17] to 30 ns [19]. On the accelerator side, two methods to increase T_{RF} are possible [24]. One makes use of single-turn extraction, which allows delivering an arbitrary pattern of beam pulses produced with a combination of bunching and chopping at the injection level (more difficult for heavy ions). The second uses multiturn extraction, followed by a subharmonic buncher that reduces the

beam repetition rate to the orbital frequency [24]. Nevertheless, in order not to disturb the optimal operation of the cyclotron, the best solution should arise from the use of fast scintillators combined with appropriate signal-processing electronics.

VI. Conclusions

We present first-measured, triple-coincidence time- and energy-correlated spectra, combined with tomographic images of the β^+ activity induced by a ^{12}C beam of 200.2 *A*MeV in a plastic phantom, indicating the feasibility of the proposed random suppression methods. However, in-beam PET during particle extraction also detects annihilation photons from short-lived β^+ emitters with high endpoint energy. Although their production cross sections are low, their influence on image blurring has to be further investigated. With the accelerator duty cycle installed at GSI, the increase in image statistics was measured to be $\leq 90\%$.

It was seen that hadrontherapy facilities based on a linear accelerator can implement in-beam PET with no need for these random suppression techniques. Synchrotron-based facilities can greatly profit from their application, and cyclotron-based facilities cannot implement in-beam PET unless random suppression is applied.

Acknowledgment

The authors would like to thank D. Schardt, S. Grözinger, and C. Bert from GSI Darmstadt for their help during the preparation and run of the experiments, P. Forck for delivering the RF signal from the synchrotron, and T. Haberer for providing the time window for these in-beam experiments.

References

[1] W. Enghardt, P. Crespo, F. Fiedler, R. Hinz, K. Parodi, J. Pawelke, and F. Pönisch, "Charged hadron tumour therapy monitoring by means of PET," *Nucl. Instrum. Methods A*, vol. 525, pp. 284–288, 2004.

[2] D. Schulz-Ertner, A. Nikoghosyan, C. Thilmann, T. Haberer, O. Jäkel, C. Karger, M. Scholz, G. Kraft, M. Wannenmacher, and J. Debus, "Carbon ion radiotherapy for chordomas and low-grade chondrosarcomas of the skull base," *Strahlenther. Onkol.*, vol. 179, pp. 598–605, 2003.

[3] D. Schulz-Ertner, A. Nikoghosyan, O. Jäkel, T. Haberer, G. Kraft, M. Scholz, M. Wannenmacher, and J. Debus, "Feasibility and toxicity of combined photon and carbon ion radiotherapy for locally advanced adenoid cystic carcinomas," *Int. J. Rad. Oncol. Biol. Phys.*, vol. 62, no. 2, pp. 391–398, 2003.

[4] J. Pawelke, W. Enghardt, T. Haberer, B. G. Hasch, R. Hinz, M. Krämer, K. Lauckner, and M. Sobiella, "In-beam PET imaging for the control of heavy-ion tumor therapy," *IEEE Trans. Nucl. Sci.*, vol. 44, no. 4, pp. 1492–1498, 1997.

[5] K. Parodi, P. Crespo, H. Eickhoff, T. Haberer, J. Pawelke, D. Schardt, and W. Enghardt, "Random coincidences during in-beam PET measurements at microbunched therapeutic ion beams," *Nucl. Instrum. Methods A*, vol. 545, pp. 446–458, 2005.

[6] W. Enghardt, P. Crespo, K. Parodi, and J. Pawelke, "Verfahren zur Korrektur der beim Monitoring der strahlentherapeutischen Behandlung mittels in-beam PET erhaltenen Messwerte" (in German), *Deutschen Patent- und Markenamt München*, no. 10 2004 009 784.4, Feb. 2004.

[7] R. D. Badawi, P. K. Marsden, B. F. Cronin, J. L. Sutcliffe, and M. N. Maisey, "Optimization of noise-equivalent count-rates in 3D PET," *Phys. Med. Biol.*, vol. 41, pp. 1755–1776, 1996.

[8] P. Crespo, J. Pawelke, and W. Enghardt, "A CAMAC data acquisition system for multi-parameter measurements,", Wiss.-Tech. Ber. FZR-372 (Annu. Rep. 2002), 2003.

[9] H. Frais-Kölbl, E. Griesmayer, H. Kagan, and H. Pernegger, "A fast low-noise charged-particle CVD diamond detector," *IEEE Trans. Nucl. Sci.*, vol. 51, no. 6, pp. 3833–3837, 2004.

[10] M. Kapusta, P. Crespo, D. Wolski, K. Heidel, L. Heinrich, J. Hutsch, J. Pawelke, M. Sobiella, A. Trzcińska, M. Moszyński, and W. Enghardt, "The LSO/APD array as a possible detector for in-beam PET in hadron therapy," *IEEE Trans. Nucl. Sci.*, vol. 51, no. 4, pp. 1389–1394, 2004.

[11] P. Crespo, M. Kapusta, J. Pawelke, M. Moszyński, and W. Enghardt, "First in-beam PET imaging with LSO/APD-array detectors," *IEEE Trans. Nucl. Sci.*, vol. 51, no. 5, pp. 2654–2661, 2004.

[12] T. Haberer, W. Becher, D. Schardt, and G. Kraft, "Magnetic scanning system for heavy ion therapy," *Nucl. Instrum. Methods A*, vol. 330, pp. 296–305, 1993.

[13] P. Crespo, "Optimization of an in-beam positron emission tomograph for monitoring heavy ion tumor therapy," Ph.D. dissertation, Darmstadt Univ. Technol., Darmstadt, Germany, 2005, submitted for publication.

[14] F. Pönisch, K. Parodi, B. G. Hasch, and W. Enghardt, "The modeling of positron emitter production and PET imaging during carbon ion therapy," *Phys. Med. Biol.*, vol. 49, pp. 5217–5233, 2004.

[15] G. Gunzert-Marx, "Nachweis leichter Fragmente aus Schwerionenreaktionen mit einem BaF_2-Teleskop-Detektor," Ph.D. dissertation, Darmstadt Univ. Technol., Darmstadt, Germany, 2004.

[16] U. Amaldi, P. Berra, K. Crandall, D. Toet, M. Weiss, R. Zennaro, E. Rosso, B. Szeless, M. Vretenar, C. Cicardi, C. D. Martinis, D. Giove, D. Davino, M. R. Masullo, and V. Vaccaro, "LIBO—A linac-booster for proton therapy: Construction and tests of a prototype," *Nucl. Instrum. Methods A*, vol. 521, pp. 512–529, 2004.

[17] A. B. Rosenfeld, P. D. Bradley, I. Cornelius, G. I. Kaplan, B. J. Allen, J. B. Flanz, M. Goitein, A. Van Meerbeeck, J. Schubert, J. Bailey, Y. Tabkada, A. Maruhashi, and Y. Hayakawa, "New silicon detector for microdosimetry applications in proton therapy," *IEEE Trans. Nucl. Sci.*, vol. 47, no. 4, pp. 1386–1394, 2000.

[18] [Online]. Available: http://abe.web.psi.ch/accelerators/ringcyc.html

[19] G. A. P. Cirrone, , Laboratori Nazionali del Sud—INFN, private communication, 2004.

[20] H. Eickhoff, R. Bär, A. Dolinskii, T. Haberer, B. Schlitt, P. Spiller, and U. Weinrich, "HICAT—The German hospital-based light ion cancer therapy project," in *Proc. Particle Accelerator Conf.*, Portland, OR, May 2003, pp. 694–698.

[21] T. Furukawa, K. Noda, E. Urakabe, M. Muramatsu, M. Kanazawa, and K. Maeda, "Characteristics of fast beam switching for spot scanning," *Nucl. Instrum. Methods A*, vol. 503, pp. 485–495, 2003.

[22] G. Coutrakon, J. Hubbard, J. Johanning, G. Maudsley, T. Slaton, and P. Morton, "A performance study of the Loma Linda proton medical accelerator," *Med. Phys.*, vol. 21, no. 11, pp. 1691–1701, 2004.

[23] H. Pernegger, H. Frais-Kölbl, E. Griesmayer, and H. Kagan *et al.*, "Design and test of a high-speed single-particle beam monitor," *Nucl. Instrum. Meth. A*, vol. 535, pp. 108–114, 2004.

[24] S. Brandenburg and L. de Vries, "A subharmonic buncher for the AGOR cyclotron," in *Proc. 15th Int. Conf. Cyclotrons, Appl.*, E. Baron and M. Lieuvin, Eds., Caen, France, Jun. 1998, pp. 193–195.